The published version of the paper "Elisabetta Cattoni, Diana Salciarini, Claudio Tamagnini (2019). A generalized Newmark Method for the assessment of permanent displacements of flexible retaining structures under seismic loading conditions. SOIL DYNAMICS AND EARTHQUAKE ENGINEERING - vol. 117 - pp. 221-233." is available at: https://doi.org//10.1016/j.soildyn.2018.11.023

A Generalized Newmark Method for the assessment of permanent displacements of flexible retaining structures under seismic loading conditions

Elisabetta Cattoni[a,*], Diana Salciarini[b], Claudio Tamagnini[b]

[a] *Università degli Studi e–Campus, Novedrate, Italy*
[b] *Università degli Studi di Perugia, Perugia, Italy*

Abstract

In recent years, much attention has been paid to performance–based design of flexible retaining structures, focusing on the evaluation of the permanent deformations of the soil–structure system caused by given seismic loads, rather than on the assessment of conventional safety factors determined by comparing seismic actions and system resistance (typically based on limit equilibrium methods). While only a few examples of fully coupled, dynamic numerical simulations of flexible retaining structures adopting advanced cyclic/dynamic models for soils can be found in literature, a number of recent works have proposed simple modifications of the classical Newmark method to assess the permanent displacements of the structure at the end of the seismic excitation. Most of the aforementioned works refer to cantilevered diaphragm walls, for which the failure mechanisms at limit equilibrium are relatively simple to describe. However, this is not the case for anchored or propped flexible structures, where the velocity field at failure under a pseudo–static seismic load is quite complex and can be affected by the plastic yielding of the wall upon bending. In this work, upper– and lower–bound limit analysis FE solutions are used as a basis for the development of a Generalized Newmark Method, based on the accurate

* *Corresponding author.*
Email addresses: `elisabetta.cattoni@uniecampus.it` (Elisabetta Cattoni), `diana.salciarini@unipg.it` (Diana Salciarini), `claudio.tamagnini@unipg.it` (Claudio Tamagnini)

evaluation of the critical accelerations for the retaining structure and the corresponding failure mechanisms. It can be shown that, under two reasonable simplifying assumptions, a Newmark–like scalar dynamic equation of motion can be derived which, upon double integration in time, provides the magnitude of the permanent displacements associated to each failure mechanism, as provided by limit analysis. This procedure allows the reconstruction of the full permanent displacement field around the excavation, not just the evaluation of horizontal soil movements at selected points. The application of the method to a number of selected prototype excavations demonstrates the potentiality of the proposed approach, which can be extended easily to other complex geotechnical structures.
Keywords: Performance–based design, Limit Analysis, Flexible retaining structures

---

List of symbols

$\mathcal{B}$	Domain considered in FE–LA simulations.
$\mathcal{B}_f$	Part of $\mathcal{B}$ interested by the failure mechanism.
$\partial\mathcal{B}_f$	Boundary of $\mathcal{B}$.
$\mathcal{I}_k$	k–th time interval for Newmark's integration.
γ	Soil weight per unit volume.
δ	Soil–wall interface friction angle.
ρ	Soil mass per unit volume.
ϕ	Soil friction angle.
ψ	Soil dilatancy angle.
$\boldsymbol{\eta}^{(+)}$, $\boldsymbol{\eta}^{(-)}$	Normalized velocity fields associated to the two possible collapse mechanisms.
a_c	Critical pseudo–static acceleration.
a_x	Horizontal component of acceleration at the bedrock.
d	Embedment depth.
D	Soil damping coefficient.

G	Soil shear modulus.
G_0	Soil small–strain shear modulus.
$G_{0,\mathrm{ref}}$	Reference value for the small–strain shear modulus.
g	Modulus of gravity acceleration.
h	Height of the excavation.
$k_c^{(-)}$, $k_c^{(+)}$	Critical seismic coefficents for the two possible directions of the pseudostatic seismic action.
k_x	Horizontal seismic coefficient at the bedrock.
q	Uniform lateral surcharge load.
$u^{(+)}$, $u^{(-)}$	Newmark displacements for the two possible directions of the pseudostatic seismic action.
$u_{x,\mathrm{max}}$	Absolute maximum permanent displacement.
$v_{\mathrm{rel}}^{(+)}$, $v_{\mathrm{rel}}^{(-)}$	Newmark relative velocities for the two possible directions of the pseudostatic seismic action.
I_A	Arias intensity.
M	Total mass of $\mathcal{B}_f$.
M_y	Yield bending moment of the wall section.
Q_x	Horizontal component of the resultant normalized momentum of $\mathcal{B}_f$.
T_d	Duration of earthquake excitation.
$U^{(+)}$, $U^{(-)}$	Scaling factors for the permanent displacement fields associated to the two possible collapse mechanisms.
$V^{(+)}$, $V^{(-)}$	Scaling factors for the normalized velocity fields $\boldsymbol{\eta}^{(+)}$ and $\boldsymbol{\eta}^{(-)}$.
$\boldsymbol{a}$	Soil acceleration vector.
$\boldsymbol{a}_b$	Acceleration vector at the bedrock.
$\boldsymbol{e}_e^{(+)}$, $\boldsymbol{e}_e^{(-)}$	Unit vectors in the two possible directions of the pseudostatic seismic action.
$\boldsymbol{f}^e$	Pseudo–static seismic action per unit volume.

$\boldsymbol{f}_c^e$ Critical value of the pseudo–static seismic action per unit volume.

$\boldsymbol{u}^{(+)}$, $\boldsymbol{u}^{(-)}$ Permanent displacement fields associated to the two possible directions of the pseudostatic seismic action.

$\boldsymbol{u}$ Soil displacement vector.

$\boldsymbol{u}_b$ Displacement vector at the bedrock.

$\boldsymbol{u}_r$ Relative displacement vector.

$\boldsymbol{u}_{\mathrm{ps}}$ post–seismic displacement field.

$\boldsymbol{v}$ Soil velocity vector.

$\boldsymbol{v}^{(+)}$, $\boldsymbol{v}^{(-)}$ Velocity fields associated to the two possible collapse mechanisms.

$\boldsymbol{v}_r$ Relative velocity vector.

$\boldsymbol{B}$ Resultant of gravity forces on $\mathcal{B}_f$.

$\boldsymbol{I}$ Resultant of inertia forces on $\mathcal{B}_f$.

$\boldsymbol{I}_f$ Resultant of inertia forces on $\mathcal{B}_f$ at failure.

$\boldsymbol{T}$ Resultant of contact forces on $\partial\mathcal{B}_f$.

$\boldsymbol{T}_f$ Resultant of contact forces on $\partial\mathcal{B}_f$ at failure.

1. Introduction

In the seismic design of flexible retaining structures, such as cantilevered or propped diaphragm walls, standard "force–based" pseudo–static design approaches – relying on on suitable modifications of classical earth pressure theories [1, 2] and limit equilibrium methods – are still widely used. In such approaches, the safety of the structure is assessed by comparing the destabilizing "loads" (typically forces or moments) acting on the structure to the system capacity for each possible failure mechanism. Safety levels are incorporated in the analysis by factorizing destabilizing actions and resistances with global or partial safety factors.

In recent years, a new approach to the design of earth retaining structures based on the concept of "performance–based design" has been given much attention, both by the research community and by the governmental agencies in charge of drafting building codes [3, 4]. This "displacement–based" approach focuses on the evaluation of the permanent deformations of the soil–structure system under a given seismic input. The rationale behind this alternative design philosophy is that: i) the seismic response of a retaining structure is not only affected by the peak ground acceleration but also by the duration and frequency content of the seismic input; and, ii) the performance of the soil–structure system can still be considered satisfactory even if limit equilibrium conditions are reached during the shaking, provided that this happens for sufficiently short time intervals, so that the permanent displacements accumulated during these periods remain below an acceptable threshold.

The current state of development of advanced numerical methods for the solution of non–linear geomechanics problems, with the parallel development of advanced inelastic constitutive equations for modeling the cyclic/dynamic behavior of soils, suggest that a possible approach to the evaluation of the seismic performance of flexible retaining structures could be the direct numerical solution of the balance of mass and momentum equations for the retaining structure and the surrounding soils, modeled as a (possibly inelastic and multiphase) continuous medium.

Examples of such an approach are provided by the works of Iai et al. [5], Alyami et al. [6], Miriano et al. [7] and Cattoni and Tamagnini [8]. However, the application of this methodology to current engineering practice is still impracticable, due to the following reasons: i) the difficulties inherent to developing robust and accurate integration strategies for complex incrementally nonlinear constitutive equations; ii) advanced inelastic models capable of capturing the details of the cyclic response of the soil typically require the calibration of large number of model constants and the definition of the initial values of (oftentimes tensorial) internal state variables adopted to provide sufficient memory of the previous loading history; iii) the lack of a commonly accepted ground concerning the minimum level of complexity in the constitutive description of soil behavior required to provide reliable predictions of the seismic performance of the retaining structure.

A possible simplification with respect to advanced numerical methods based on the principles of continuum mechanics and computational inelasticity, is provided by the attempts to extend the classical Winkler approach for flexible retaining structures (see, *e.g.*, ref. [9]) to earthquake loading conditions. Notable examples in this field are provided by the works of Franchin and coworkers [10, 11, 12]. Although they still have a strong appeal to practitioners, these Winkler–type models suffer from some important drawbacks when applied to the analysis of SSI problems for flexible retaining structures. The calibration of the subgrade reaction modulus from standard geotechnical site investigations – in which the in–situ and laboratory test data are interpreted under the assumption that the soil is a continuous medium – is typically based on empirical rules or very strong simplifying assumptions. Moreover, the limiting values of the subgrade reactions in compression and in extension are derived from classical earth pressure theories, developed from highly idealized wall failure mechanisms. Finally, being the model focused on the structural elements, the inertial properties of the soil behind and in front of the wall are usually accounted for in a drastically simplified manner.

An alternative, much simpler strategy is based on ad–hoc modifications of the classical Newmark sliding block method [13], where permanent displacements can be obtained as the result of a double integration of the equations of motion for an assumed failure mechanism, when a (critical) acceleration threshold is exceeded. Key points in this procedure are the accurate evaluation of the critical acceleration a_c – *i.e.*, the soil acceleration which generates pseudo–static inertia forces capable of bringing the soil–retaining structure system in a limit equilibrium condition, such as horizontal sliding of gravity walls or rotation of flexible embedded walls around a fixed point – and the proper definition of the failure mechanism for the soil–structure system. Examples of calculation of permanent displacements with this type of approach can be found, *e.g.*, in Refs. [14, 15, 16, 17, 18, 19] for relatively rigid gravity walls, and [15, 20, 21, 22, 23] for flexible structures such as anchored bulkheads and diaphragm walls.

As far as anchored diaphragm walls are concerned, the application of Newmark approach presents two main problems: the calculation of the critical acceleration by means of classical limit equilibrium solutions could be inaccurate, due to the numerous simplifying assumptions introduced in the analysis, and the accurate definition of the collapse mechanism is by no means trivial, given that no simple equivalent "block sliding" mechanism can be identified, particularly when wall yielding occurs.

In a recent paper, Cattoni and Tamagnini [24] have shown how the use of the theorems of Limit Analysis by means of suitable Finite Element implementations (FE–LA) can provide an accurate and versatile solution to the aforementioned problems, since critical accelerations and the associated collapse mechanisms can be determined very effectively as a function of the problem geometry and the mechanical properties of the soil and the structural elements.

In this paper, the work of Cattoni and Tamagnini is extended to show how a Generalized Newmark Method (GNM) for the simplified evaluation of earthquake–induced permanent soil and structural displacement can be constructed, based on the results of FE–LA simulations, with particular reference to embedded r.c. diaphragm walls.

The main steps of the procedure can be summarized as follows:

1. the upper– and lower–bound theorems of Limit Analysis are used to identify the critical accelerations corresponding to pseudo–static inertial force fields with a given orientation (typically horizontal) and 2 possible directions (positive or negative with respect to the x–axis of the global reference frame, assumed as horizontal);
2. the upper–bound (kinematic) solution of LA is used to identify, as accurately as possible, the velocity fields associated to the two collapse mechanisms, denoted by $\boldsymbol{v}^{(+)}(\boldsymbol{x})$ and $\boldsymbol{v}^{(-)}(\boldsymbol{x})$, respectively;
3. using the analogy between the motion of the soil volume affected by the collapse mechanism and the sliding of a rigid block on a horizontal plane

when the inertia forces exceed the limit equilibrium conditions, the permanent displacement fields associated to the two collapse mechanisms, $\boldsymbol{u}^{(+)}(\boldsymbol{x}, t)$ and $\boldsymbol{u}^{(-)}(\boldsymbol{x}, t)$, are computed using a standard Newmark–type procedure, and then vectorially composed to obtain the total permanent displacement field at the generic time $t \in [0, T_d]$.

The post–seismic displacement field is then obtained as:

$$\boldsymbol{u}_{\mathrm{ps}}(\boldsymbol{x}) = \boldsymbol{u}(\boldsymbol{x}, T_d) \tag{1}$$

where T_d is the duration of the earthquake excitation.

In Step 1 of the proposed method, the critical accelerations are established for the failure mechanisms provided by pseudo–static loads, as in classical Newmark approaches. This procedure shares some similarities to structural earthquake engineering applications in which the base–shear capacity of a structure provided by a single–mode pushover analysis is used in the response history analysis of an equivalent nonlinear SDOF system. In this case, the limitations of this approach have been pointed out, *e.g.*, by Villaverde [25]. Goulet et al. [26] have shown that different ground motion time–series may induce different failure mechanisms in a framed structure. The real extent to which such limitations also apply to the collapse of geotechnical systems such as propped diaphragm walls is an open question, which will require a thorough investigation on the failure modes activated under different earthquake loading conditions by means of advanced numerical simulations, and, as such, falls beyond the scope of the present work.

The outline of the paper is as follows. Sect. 2 presents the application of FE–LA for the evaluation of the critical accelerations and the kinematic features of the computed collapse mechanisms for 6 retaining structures, differing for soil conditions, wall geometry and wall structural properties. The basis of the Generalized Newmark Method are detailed in Sect. 3. The application of the method to the structures considered in Sect. 2 is presented in Sect. 4. The comparison between the results obtained with the Generalized Newmark Method and non–linear dynamic FE simulations for a retaining structure subjected to two different acceleration histories is presented in Sect. 5, to provide a validation for the proposed simplified approach. Finally, some concluding remarks are provided in Sect. 6.

2. Critical seismic conditions of propped diaphragm walls

As shown by [24], FE limit analysis [27, 28] is a versatile and accurate tool for determining the pseudostatic critical acceleration of deep excavations supported by diaphragm walls and the corresponding collapse mechanism. This approach, implemented in the commercial FE code OptumG2 [29], has been adopted to evaluate the seismic performance of a number of deep excavations in cohesionless sands with height $h = 8$ m, supported by diaphragm walls propped at the crest, under seismic excitations differing for PGA and Arias Intensity I_A.

2.1. Problem geometry, material properties and simulations program

The geometry of the problem under study is shown in Fig. 1. In the application of LA for the definition of failure conditions under pseudo–static seismic loads, the soil has been assumed as a rigid–perfectly plastic material with Mohr–Coulomb yield condition and non–associative plastic flow. The walls, modeled as 1–dimensional beam elements, have been assumed as rigid–perfectly plastic solids, with yield bending moment M_y.

In order to identify the different collapse mechanisms involving soil and (possibly) structural yield, six problems have been considered, with varying wall embedment depth d, soil friction angle ϕ and wall yield bending moment M_y. In two cases, a uniform lateral surcharge load $q = 50$ kPa has been applied on the right side of the excavation, in order to have non–symmetrric collapse mechanisms for the two possible orientations of the pseudo–static seismic force.

A detail of the FE discretization used for the LA simulations is shown in Fig. 2. 3–noded linear stress triangles have been used in Lower Bound calculations, while Upper Bound simulations have been made with 3–noded linear

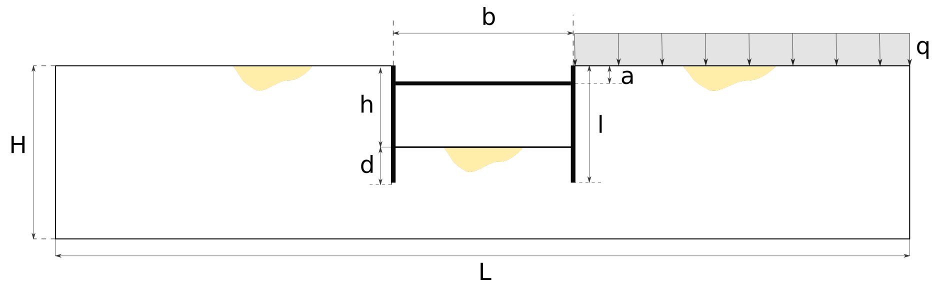

Figure 1: Problem geometry.

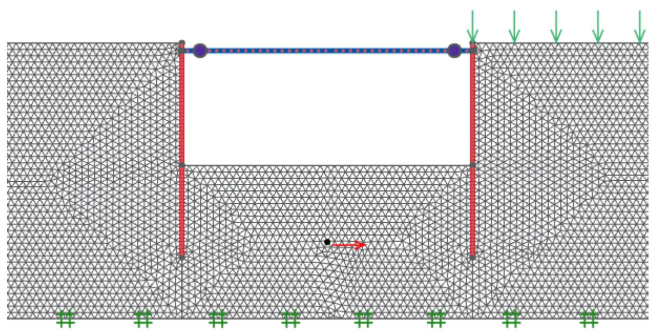

Figure 2: Detail of the FE–LA discretization of simulation r06, close to the excavation.

displacement elements. Although the code allows for mesh refinement in zones of high plastic strain concentration, a uniform discretization with 15144 very small elements has been adopted for the soil to allow the superposition of the collapse mechanisms obtained with seismic forces of different orientation. The large number of elements has provided the required level of accuracy in the computed solution, at expense of some computational efficiency loss.

The details of the simulation program, with the geometry and the mechanical properties of the soil and the structural elements, are given in Tab. 1. In the table, information are also provided for one additional simulation (r07, discussed in Sect. 5), performed to validate the Generalized Newmark Method (Sect. 4).

In the simulations r01–r06, wall embedment depths d of 4 and 6 m have been considered, with embedment ratios d/h varying from 0.5 to 0.75. The excavation width b has been set to 18 m for all the cases examined. The soil unit weight γ has been assumed constant and equal to 18 kN/m^3 in all the cases considered, while the friction angle has been varied between 26 and 35 degrees. To account for non–associative plastic flow at failure, a constant dilatancy angle $\psi = 15°$ has been adopted.

It is well known that Limit Analysis relies crucially on the concept of associated flow rule. However, for granular materials, this assumption is, in many cases, not supported by experimental evidence. To extend the FE–LA procedures to the case of non-associative cohesive-frictional materials, Krabbenhoft *et al.* [30] have proposed a general approach in which the original non–associated problem is transformed into an associated one by replacing the actual soil strength properties, c and ϕ, with equivalent ones, c^*, ϕ^*, which are functions of c and ϕ, as well as of the dilatancy angle ψ. This approach has been used in this work. It is worth noting that Cattoni and Tamagnini [24] have investigated the effect of non–associativeness on the critical acceleration a_c of propped diaphragm walls and, from the results of an extensive parametric study, have observed that the dilatancy angle has only a minor impact on the computed values of a_c.

A soil–wall interface friction angle, δ, equal to 50% of the soil friction angle ϕ has been considered to take into account wall friction. Finally, the yield bending moment M_y of the two walls has been varied in the range 800 kNm/m (low strength, typical of slender sheetpiles) to 2400 kNm/m (high strength, typical of r.c. diaphragm walls), see ref. [24].

2.2. Collapse mechanisms and critical accelerations

The different collapse mechanisms obtained in the six cases considered, for pseudostatic forces oriented either in the positive (+) or negative (−) direction of the x–axis of the global reference frame (Fig. 1), are shown in Fig. 3. In the following we will refer to the wall directly affected by the seismic action

Table 1: Program of LA–FE simulations.

run	d	d/h	γ	ϕ	ψ	δ	M_y	q
#	(m)	(–)	(kN/m^3)	(deg)	(deg)	(deg)	(kNm/m)	(kPa)
r01	4	0.50	18	30	15	15	2400	0
r02	4	0.50	18	30	15	15	1200	0
r03	4	0.50	18	35	15	17.5	800	0
r04	6	0.75	18	30	15	15	800	0
r05	6	0.75	18	26	15	13	1200	50
r06	6	0.75	18	26	15	13	800	50
r07	3	0.38	18	30	15	30	2400	0

(left wall for positive pseudo–static force, right wall for negative pseudo–static force) as "leading wall" and to the wall on the opposite side of the excavation as "trailing wall".

The collapse mechanisms for positive and negative directions of the pseudo–static force are symmetric for simulations r01 to r04, while the presence of the surcharge load in cases r05 and r06 makes the negative failure mechanism different from the positive one. Case r01 is the only one in which plastic yielding occurs only in the soil mass, and no plastic hinges form in the two walls. Only the leading wall is actually rotating around the point of contact with the strut. No plastic zones form behind the trailing wall.

In cases r02 and r03, the leading wall translates and rotates remaining rigid, while the trailing wall and the soil behind it, pushed by the strut, yield with the formation of a plastic hinge located at about half the excavation depth. In case r04, where the wall yield bending moment is minimum and soil shear strength is relatively low, both walls undergo plastic yielding. In cases r05 and r06, the

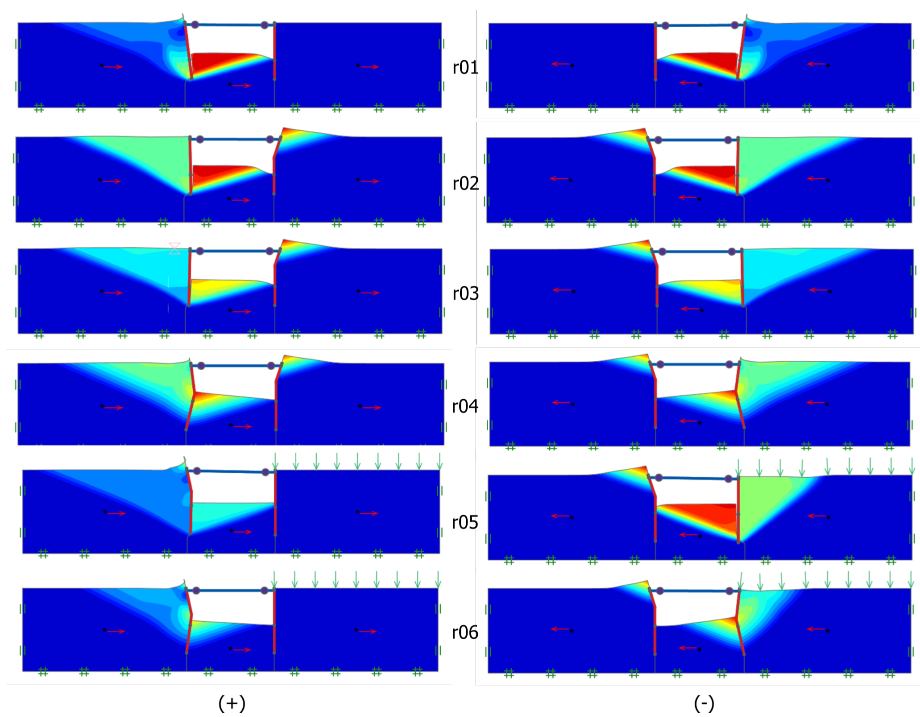

Figure 3: Contour maps of normalized velocity magnitude. Left column: positive pseudostatic force; right column: negative pseudostatic force.

collapse mechanisms for the (+) and (−) earthquake directions are significantly different, due to the presence of the surcharge load on the right side of the excavation. When the pseudo–static force acts on the positive direction, the leading wall fails while the trailing wall remains still. In the other case, what happens to the leading wall depends on M_y, while the trailing wall always yields as in cases r02 and r03. It is important to note that the plastic mechanisms activated in the soil by the two earthquake loadings affect zones of soil which are not disjoint: the permanent displacement fields produced by the (+) and (−) mechanisms interact with each other in all the cases considered.

A summary of the critical seismic coefficients obtained in each simulation is given in Tab. 2. For symmetric plastic mechanisms (r01–r04) the critical accelerations computed for both directions in the lower bound (LB) and upper bound (UB) simulations are the same, within a small approximation due to the non perfect symmetry of the unstructured mesh. The presence of surcharge load makes the value of $k_c^{(-)}$ much smaller than $k_c^{(+)}$. The differeces between the UB and LB solutions are very small, with a maximum error smaller than 5% of the average value for each of the 12 simulations considered. Therefore, to all practical purposes, the average values of k_c listed in the last two columns of Tab. 2 can be used as the critical seismic coefficients for each failure mechanism.

3. Generalized Newmark method

Let $\mathcal{B}$ be the domain occupied by the soil body and the structure under study. Both the soil and the structural elements are considered as rigid–perfectly plastic materials. Soil yielding is defined by the Mohr–Coulomb yield condition.

Let $\mathcal{B}_f$ be the part of $\mathcal{B}$ interested by the failure mechanism generated by a pseudo–static critical seismic actions whose volume density is given by:

$$\boldsymbol{f}_c^e = \rho a_c \boldsymbol{e}_e^{(i)} = k_c g \rho \boldsymbol{e}_e^{(i)} \tag{2}$$

where $k_c = a_c/g$ is the critical seismic coefficient (normalized critical acceleration) and $\boldsymbol{e}_e^{(i)}$, with $(i) = (+)$ or $(-)$ is the unit vector in the direction of the

Table 2: Critical accelerations for the 7 cases considered.

run	LB	UB	LB	UB	Average	Average
	$k_c^{(+)}$	$k_c^{(+)}$	$k_c^{(-)}$	$k_c^{(-)}$	$k_c^{(+)}$	$k_c^{(-)}$
#	(–)	(–)	(–)	(–)	(–)	(–)
r01	0.411	0.451	0.410	0.449	0.431	0.430
r02	0.406	0.425	0.405	0.424	0.415	0.415
r03	0.510	0.530	0.511	0.529	0.520	0.520
r04	0.412	0.417	0.412	0.417	0.415	0.414
r05	0.357	0.372	0.300	0.320	0.364	0.310
r06	0.314	0.322	0.231	0.247	0.318	0.239
r07	0.285	0.353	0.286	0.351	0.319	0.319

pseudo–static inertia force. Finally, let $\partial\mathcal{B}_f$ be the boundary of the volume $\mathcal{B}_f$, along which contact force densities are exchanged with the rest of the stable soil body. Without lack of generality, in the following $\boldsymbol{e}_e^{(i)}$ will be assumed as horizontal and oriented either in the positive $(+)$ or in the negative $(-)$ direction of the x–axis of the adopted global reference frame. These two choices correspond to two distinct potential plastic collapse mechanisms induced by earthquake loading, see for example Fig. 10, referring to one of the cases examined in the following Sect. 4.

For each of the two possible directions of the pseudo–static seismic action $\boldsymbol{f}^e$, the Finite Element implementation of the upper–and lower–bound theorems of limit analysis (FE–LA) provided by the code Optum G2 is used to determine:

a) the best approximation to the critical acceleration coefficients $k_c^{(+)}$ and $k_c^{(-)}$ for the positive and negative directions of the pseudo–static seismic action;

b) the normalized velocity fields, $\boldsymbol{\eta}^{(+)}(\boldsymbol{x})$ and $\boldsymbol{\eta}^{(-)}(\boldsymbol{x})$, associated to each collapse mechanism, defined as:

$$\boldsymbol{\eta}^{(+)} := \frac{\boldsymbol{v}^{(+)}}{\max\left\|\boldsymbol{v}^{(+)}\right\|} \qquad\qquad \boldsymbol{\eta}^{(-)} := \frac{\boldsymbol{v}^{(-)}}{\max\left\|\boldsymbol{v}^{(-)}\right\|} \tag{3}$$

Note that the upper–bound theorem provides the velocity fields $\boldsymbol{v}^{(+)}$ and $\boldsymbol{v}^{(-)}$ at collapse up to an arbitrary scale. The normalization conditions in eq. (3) are therefore necessary to provide a scale factor.

3.1. Equations of motion for the body $\mathcal{B}_f$

Let us consider the earthquake excitation as a prescribed horizontal acceleration time history applied at the base of the soil volume $\mathcal{B}$:

$$\boldsymbol{a}_b(t) = \ddot{\boldsymbol{u}}_b(t) = a_x(t)\boldsymbol{e}_e \tag{4}$$

the function $a_x(t)$ being provided by the input seismic accelerogram.

For a given collapse mechanism, the global equilibrium equations applied to the part $\mathcal{B}_f$ read:

$$\int_{\mathcal{B}_f} \rho\dot{\boldsymbol{v}}\,dv = \int_{\mathcal{B}_f} \rho\boldsymbol{b}\,dv + \int_{\partial\mathcal{B}_f} \boldsymbol{t}\,da \tag{5}$$

where $\boldsymbol{v}$ is the velocity field, $\boldsymbol{b}$ is the gravity force density per unit mass and $\boldsymbol{t}$ is the contact force density at the boundary of $\mathcal{B}_f$. In a more synthetic form, eq. (5) can be rewritten as:

$$\int_{\mathcal{B}_f} \rho \dot{\boldsymbol{v}}\, dv = \boldsymbol{B} + \boldsymbol{T} \tag{6}$$

where:

$$\boldsymbol{B} := \int_{\mathcal{B}_f} \rho \boldsymbol{b}\, dv \qquad\qquad \boldsymbol{T} := \int_{\partial\mathcal{B}_f} \boldsymbol{t}\, da \tag{7}$$

3.2. Relative equations of motion for the body $\mathcal{B}_f$

Let:

$$\boldsymbol{u}_r := \boldsymbol{u} - \boldsymbol{u}_b \qquad\qquad \boldsymbol{v}_r := \boldsymbol{v} - \boldsymbol{v}_b \qquad\qquad \boldsymbol{a}_r := \boldsymbol{a} - \boldsymbol{a}_b$$

be the displacement, velocity and acceleration fields relative to a reference frame moving with the base of the soil volume $\mathcal{B}$. The equations of motion (6) in the relative reference frame now read:

$$\int_{\mathcal{B}_f} \rho \dot{\boldsymbol{v}}_r\, dv = \boldsymbol{B} + \boldsymbol{T} + \boldsymbol{I} \tag{8}$$

where:

$$\boldsymbol{I}(t) := -\int_{\mathcal{B}_f} \rho \boldsymbol{a}_b(t)\, dv \tag{9}$$

is the resultant of the inertia forces acting on $\mathcal{B}_f$.

3.3. Limit equilibrium conditions

Under limit equilibrium conditions induced by inertia forces in direction $(i) = (+)$ or $(-)$, we can assume that:

$$\boldsymbol{B} + \boldsymbol{T}_f + \boldsymbol{I}_f = \boldsymbol{0} \tag{10}$$

where

$$\boldsymbol{T}_f := \int_{\partial\mathcal{B}_f} \boldsymbol{t}_f^{(i)}\, da \qquad\qquad \boldsymbol{I}_f := -\int_{\mathcal{B}_f} \rho \boldsymbol{a}_c^{(i)}\, dv \tag{11}$$

and $\boldsymbol{a}_c = -k_c^{(i)} g \boldsymbol{e}_e^{(i)}$, the minus sign indicating that the inertia forces have direction opposite to the critical acceleration.

3.4. Permanent displacement field

In order to quantify the motion of the collapsing soil mass for each potential failure mechanism (i), we introduce the following:

Assumption 1. *When the collapsing soil mass $\mathcal{B}_f$ is in motion under inertia forces larger than the critical ones – as provided by eq.* (10) *– the relative velocity field $\boldsymbol{v}_r^{(i)}$ is proportional to the normalized velocity field $\boldsymbol{\eta}^{(i)}$ according to:*

$$\boldsymbol{v}_r^{(i)}(\boldsymbol{x},t) = V^{(i)}(t)\boldsymbol{\eta}^{(i)}(\boldsymbol{x}) \tag{12}$$

where the scalar function $V^{(i)}(t)$ represents a single scaling factor for the normalized velocity field $\boldsymbol{\eta}^{(i)}$, and:

Assumption 2. *Under dynamic equilibrium conditions, the stress vector field $\boldsymbol{t}$ acting on $\partial\mathcal{B}_f$ remains equal to $\boldsymbol{t}_f^{(i)}$ since the boundary between the failing soil body and the remaining stable soil mass is a slip line.*

It is worth noting that a unique value of the scaling factor $V^{(i)}(t)$ for the entire domain $\mathcal{B}_f$ does not imply that the collapse mechanism is a pure translation, as the normalized velocity field $\boldsymbol{\eta}^{(i)}$ varies with $\boldsymbol{x}$ in both modulus and orientation.

Taking into account Assumptions 1 and 2, and eq. (10), the equation of motion under critical conditions reads, for each instant in which $\mathcal{B}_f$ is in motion:

$$\dot{V}^{(i)} \int_{\mathcal{B}_f} \rho\boldsymbol{\eta}^{(i)}\, dv = \boldsymbol{I} - \boldsymbol{I}_f = -\int_{\mathcal{B}_f} \rho \left[\boldsymbol{a}_b(t) - \boldsymbol{a}_c^{(i)}\right] dv \tag{13}$$

considering that:

$$\boldsymbol{a}_b(t) = -a_x(t)\boldsymbol{e}_e^{(i)} = -gk_x(t)\boldsymbol{e}_e^{(i)} \qquad\qquad \boldsymbol{a}_c^{(i)} = -k_c^{(i)} g\boldsymbol{e}_e^{(i)} \tag{14}$$

eq. (13) yields:

$$\begin{aligned}\dot{V}^{(i)} \int_{\mathcal{B}_f} \rho\boldsymbol{\eta}^{(i)}\, dv &= \left\{\int_{\mathcal{B}_f} \rho g \left[k_x(t) - k_c^{(i)}\right] dv\right\} \boldsymbol{e}_e^{(i)} \\ &= Mg\left[k_x(t) - k_c^{(i)}\right] \boldsymbol{e}_e^{(i)} \end{aligned}\tag{15}$$

where:

$$M := \int_{\mathcal{B}_f} \rho\, dv \tag{16}$$

is the total mass of the soil in motion (in the domain $\mathcal{B}_f$).

Projecting eq. (15) in the direction $\boldsymbol{e}_e^{(i)}$, we obtain the simplified equation of motion:

$$\dot{V}^{(i)} = \frac{Mg}{Q_x}\left[k_x(t) - k_c^{(i)}\right] \qquad \text{where:} \qquad Q_x := \int_{\mathcal{B}_f} \rho \boldsymbol{\eta}^{(i)} \cdot \boldsymbol{e}_e^{(i)}\, dv \tag{17}$$

is the horizontal component of the resultant normalized momentum of the soil in $\mathcal{B}_f$.

Obviously, in eq. (17), $\dot{V}$ can only be non–zero when $k_x(t) > k_c^{(i)}$. Integrating eq. (17) in time over the time intervals $\mathcal{I}_k$ over which either $k_x > k_c^{(i)}$ or $V > 0$ (like in Newmark's sliding block approach), we get:

$$V^{(i)}(t) = \frac{M}{Q_x}\sum_{k=1}^{n_{\text{int}}}\int_{\mathcal{I}_k} g\left[k_x(\tau) - k_c^{(i)}\right] d\tau = \frac{M}{Q_x}\, v_{\text{rel}}^{(i)}(t) \tag{18}$$

$$U^{(i)}(t) = \int_0^t V^{(i)}(\tau)\, d\tau = \frac{M}{Q_x}\int_0^t v_{\text{rel}}^{(i)}(\tau)\, d\tau = \frac{M}{Q_x}\, u^{(i)}(t) \tag{19}$$

where $v_{\text{rel}}^{(i)}(t)$ and $u^{(i)}(t)$ are the Newmark velocity and displacement resulting from the single and double time integration of the function $g(k_x(t) - k_c^{(i)})$.

The permanent displacement field at time t associated to the (i)–th plastic mechanism is given by:

$$\boldsymbol{u}_r^{(i)}(\boldsymbol{x}, t) = U^{(i)}(t)\boldsymbol{\eta}^{(i)}(\boldsymbol{x}) \tag{20}$$

The final permanent (relative) displacement field associated to both collapse mechanisms is finally computed by vectorially composing the two fields $\boldsymbol{u}_r^{(+)}(\boldsymbol{x}, t)$ and $\boldsymbol{u}_r^{(-)}(\boldsymbol{x}, t)$ at the generic time $t \in [0, T_d]$:

$$\boldsymbol{u}_r(\boldsymbol{x}, t) = \boldsymbol{u}_r^{(+)}(\boldsymbol{x}, t) + \boldsymbol{u}_r^{(-)}(\boldsymbol{x}, t) \tag{21}$$

The calculation of the two scalar quantities M and Q_x, defined by eqs. (16) and $(17)_2$, relies on the results of the Upper Bound FE simulations. First, the domain $\mathcal{B}_f$ is identified as the union of all the elements in the discretization where the average value of $\left\|\boldsymbol{\eta}^{(i)}\right\|$ is larger than a predefined (small) threshold ε , set to 10^{-3} in all the cases examined. Then, the two integrals are computed as the sum of the contributions of each element belonging to $\mathcal{B}_f$. Parametric studies conducted with different threshold values have shown that the computed values of M and Q_x do not vary significantly as ε is reduced.

4. Application to deep excavations supported by diaphragm walls

The Generalized Newmark method outlined in previous Sect. 3 has been applied to the 6 retaining structures considered in Sect. 3, adopting the acceleration time history recorded on 18.01.2017 in the site of Poggio Cancelli (L'Aquila province, Italy), taken from the accelerometric database Itaca [31]. The main properties of the earthquake record are summarized in Tab. 3, while the time history of the horizontal acceleration and the corresponding response spectrum are shown in Fig. 4. It can be observed that the spectrum is characterized by two peaks, located at about 0.2 s and 0.45 s (f = 2.22 and 5 Hz).

Table 3: Properties of the acceleration time history considered.

Station name	Date	Site class. (EC8)	M_w (–)	PGA (cm/s^2)	T_d (s)	I_A (cm/s)
Poggio Cancelli	18.01.2017	B*	5.5	575.0	31.085	195.571

4.1. Definition of the seismic input

In the application of Newmark's approach to the performance–based design of ordinary gravity walls, the seismic input considered is typically applied directly at the base of the wall, see, *e.g.*, [14]. In the case of deep excavations supported by flexible diaphragm walls, strong amplification effects may occur, depending on the stratigraphy and the mechanical properties of the soil layers affected. This must be taken into account in the selection of the accelerograms used to compute the permanent displacement field using the procedure discussed in Sect. 3.

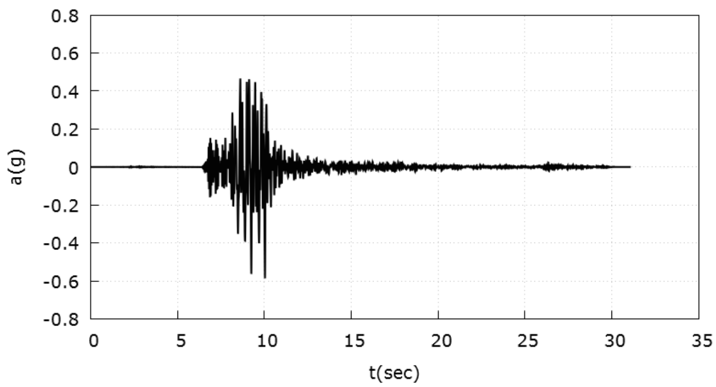

(a)

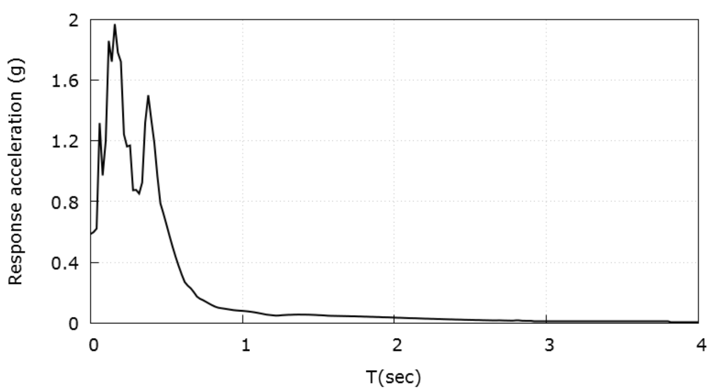

(b)

Figure 4: Poggio Cancelli earthquake record: a) time history of the acceleration; b) response spectrum at 5% damping.

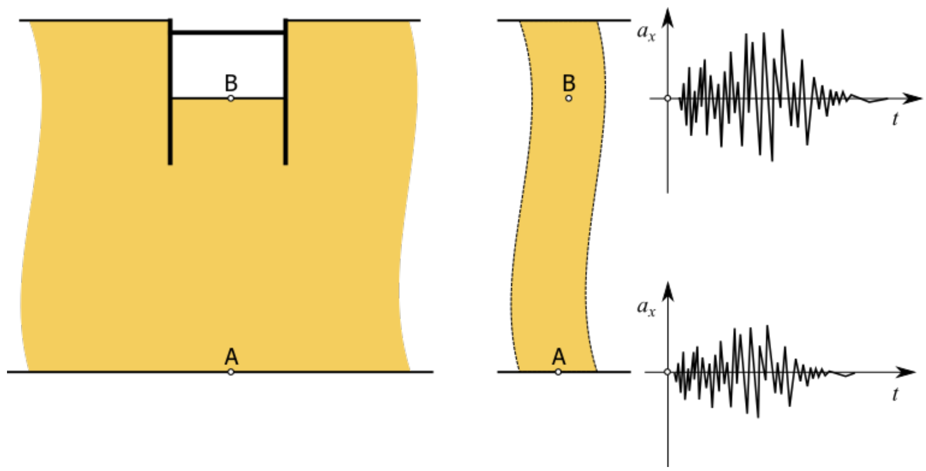

Figure 5: Definition of the seismic input via a 1–d site response analysis

Following Callisto and Soccodato [20], a possible simplified strategy to take this effect into account, which appears consistent with the scope of the Generalized Newmark approach, is to evaluate the local amplification effects by means of a simplified 1–d nonlinear site response analysis, using one of the tools widely available for this purpose. In this work, we have used the code EERA [32]. In principle, an equivalent, or average, acceleration time history should be used to account for the spatial variability of the acceleration within the moving soil mass. In practice, a reasonable approximation consists in considering the acceleration history computed at a depth equal to the excavation height h, as shown in Fig. 5.

The mechanical characterization of the soil layer in terms of strain–dependent stiffness and damping has been carried out considering two possible cases: a relatively stiff, class B soil and a relatively soft, class C soil according to the site classification of the Italian building code [4]. The small strain shear modulus G_0 has been assumed to depend on mean effective stress p according to the following relation [33]:

$$G_0 = G_{0,\mathrm{ref}} \sqrt{\frac{p}{p_{\mathrm{ref}}}} \tag{22}$$

In eq. (22) the effects of soil preconsolidation on G_0 have been neglected, as-

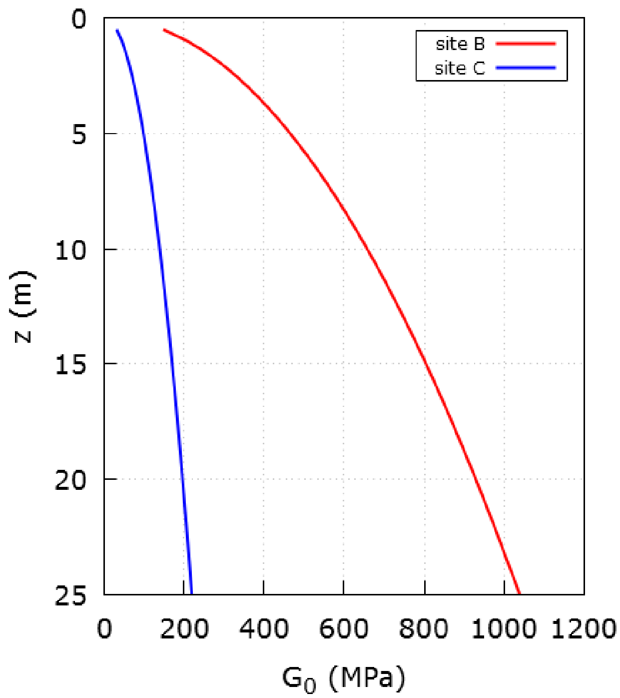

Figure 6: Profiles of small–strain shear modulus G_0 assumed for soils type B and C.

suming OCR = 1. The profiles of G_0 with depth assumed for the two cases considered are shown in Fig. 6.

The evolution of shear stiffness and damping for the two sites have been defined using a simplified version of the relations proposed by Ishibashi and Zhang [34]:

$$\frac{G}{G_0} = \frac{1}{2}\left\{1 + \tanh\left[\ln\left(\frac{0.000102}{\gamma}\right)^{0.492}\right]\right\} \tag{23}$$

$$D = 0.333\left[0.586\left(\frac{G}{G_0}\right)^2 - 1.547\left(\frac{G}{G_0}\right) + 1\right] \tag{24}$$

The functions $G(\gamma)$ and $D(\gamma)$ of eqs. (23) and (24) are shown in Fig. 7.

The response spectra for the seismic input at the base and for the two accelerograms computed at a depth h for soil profiles B and C are shown in Fig. 8.

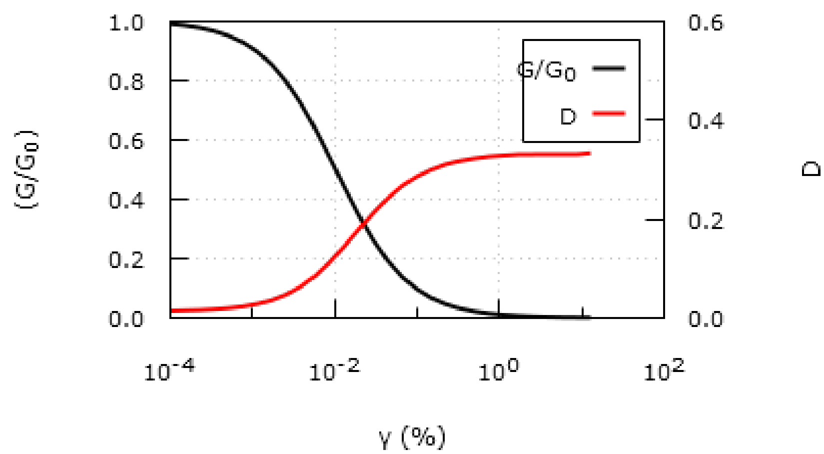

Figure 7: Shear stiffness decay curve (a) and damping ratio (b) *vs.* shear strain relation assumed in 1–d site response simulations.

A significant amplification of the spectral ordinates is clearly visible for both sites. As expected, the amplification effect, in terms of acceleration magnitude, is slightly larger for site C. However, it is interesting to note that the different soil profiles amplify only one of the two dominant frequencies of the seismic input: the higher dominant frequency is amplified by soil profile B, while the opposite occurs for soil profile C. This is due to the fact that the fundamental periods of the two deposits are equal to 0.171 s for site B and 0.373 s for site C.

4.2. Results

The 2 acceleration time histories obtained by this procedure for sites B and C, as well as the original seismic record from Poggio Cancelli have been applied to all the 6 cases of deep excavations presented in Sect. 2. The computed values of the masses $M^{(+)}$ and $M^{(-)}$, and of the resultant normalized momenta in the horizontal direction, $Q_x^{(+)}$ and $Q_x^{(-)}$, for all the simulations are reported in Tab. 4. It is worth noting that, as expected, the values of M and Q_x corresponding to the $(+)$ and $(-)$ collapse mechanisms are almost equal for

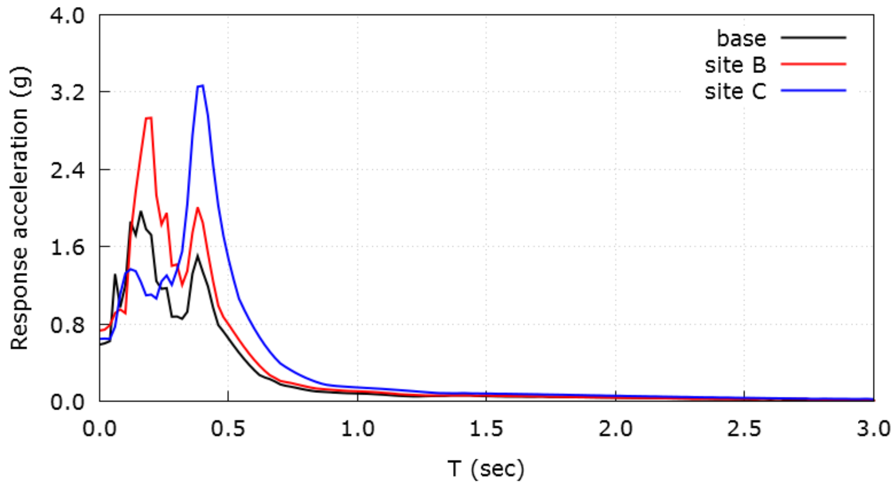

Figure 8: Response spectra for the seismic input at the base and for the accelerograms computed at a depth h for soil profiles B and C.

symmetrically loaded structures (cases r01–r04) and significantly different for the non–symmetrically loaded structures (cases r05 and r06).

An example of the results obtained by applying the Generalized Newmark method to case r06 and soil profile C is provided in Figs. 9 to 13. The results of the Newmark integration procedure for the (+) and (−) directions of the seismic action, computed for case r06, are shown in Fig. 9. It can be noticed that, due to the presence of the surcharge load, the critical accelerations are not the same for the two collapse mechanisms, a_c of the (−) case being smaller than the one calculated for the (+) case.

Fig. 10 plots the plastic regions associated to the two collapse mechanisms, over which the two quantities M and Q_x are calculated, see eqs. (16) and (17). It is worth noting that the two regions overlap beneath the bottom of the excavation and in the zone of soil behind the upper part of the left wall, which undergoes a "passive" failure in the (−) mechanism due to the thrust exerted by the strut on the left wall. The computed values of the ratios Mg/Q_x for the two collapse mechanisms are 6.53 and 5.15, respectively.

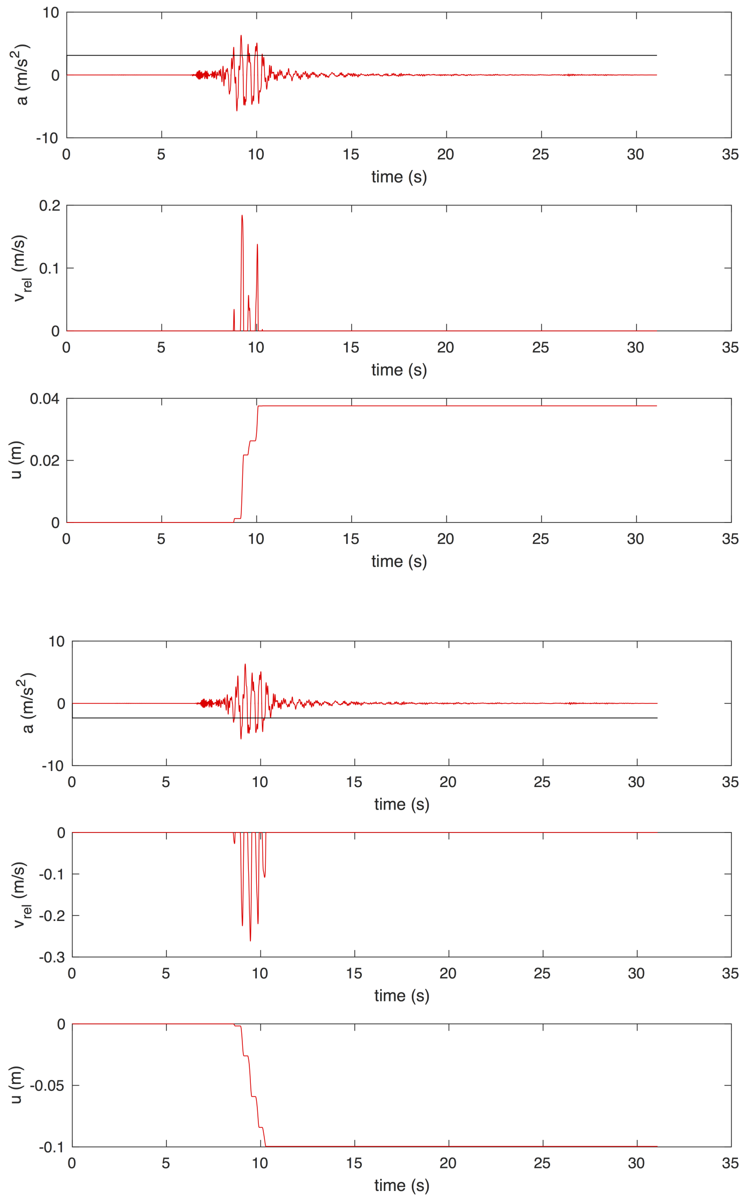

Figure 9: Simulation r06: Newmark integration for the two collapse mechanisms.

Table 4: Computed values of $M^{(+)}$, $M^{(-)}$, $Q_x^{(+)}$ and $Q_x^{(-)}$ for the 6 cases considered.

run	$M^{(+)}$	$M^{(-)}$	$Q_x^{(+)}$	$Q_x^{(-)}$
#	(t)	(t)	(t)	(t)
r01	515.02	505.67	108.60	105.68
r02	662.00	571.62	176.18	173.53
r03	579.22	580.77	131.94	132.48
r04	631.12	638.84	146.17	145.50
r05	665.59	543.51	117.87	187.92
r06	485.23	407.65	74.28	79.16

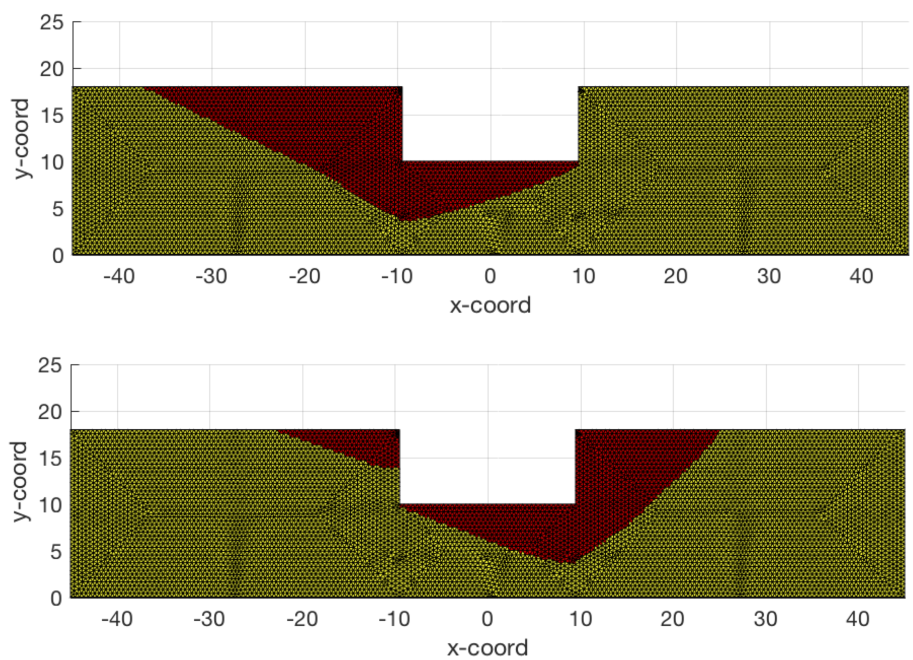

Figure 10: Simulation r06, soil profile C: plastic regions for the two collapse mechanisms.

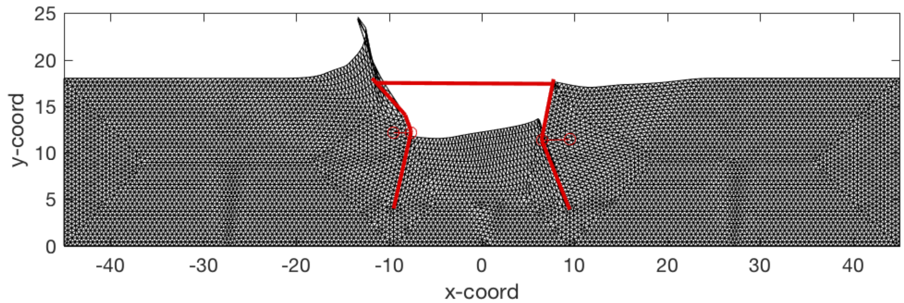

Figure 11: Simulation r06, soil profile C: deformed mesh for the combined displacement field.

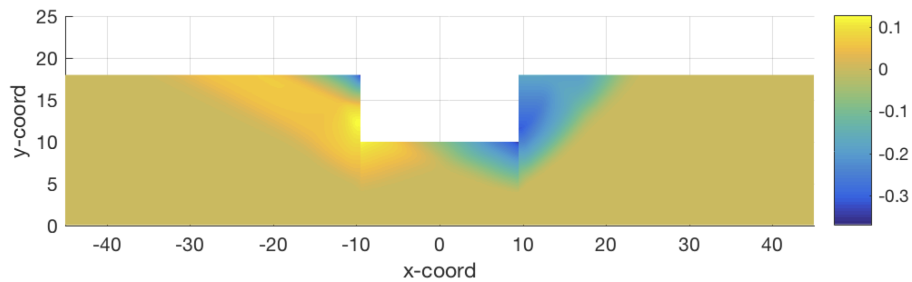

Figure 12: Simulation r06, soil profile C: contour maps of horizontal displacement u_x.

The permanent displacement field provided by eq. (21) is shown by the deformed mesh reported in Fig. 11. The contour map of the horizontal displacements is given in Fig. 12. The points where the maximum (positive) and minimum (negative) horizontal displacements occur are marked in Fig. 11 with red open circles. In both cases they are close to the plastic hinges formed in the two walls. In the particular case considered, the interaction between the failure mechanisms associated with the two possible orientations of the seismic action is significant. The permanent displacement field cannot be accurately predicted by considering each wall independently, with the seismic action oriented towards the excavation.

A summary of the results obtained in the 6 cases considered and with seismic inputs corresponding to no site amplification, site B and site C, is

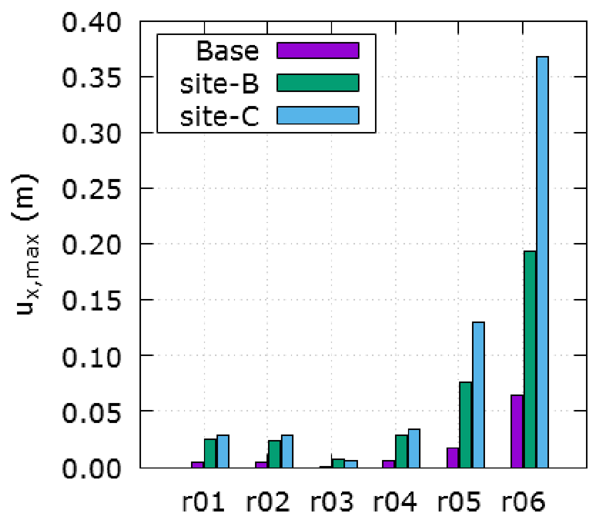

Figure 13: Maximum permanent horizontal displacements for seismic inputs a1–a4.

provided by Fig. 13 in terms of absolute maximum permanent displacement $u_{x,\max} = \max(|u_x|)$. As expected, the higher the critical acceleration, the lower is the computed permanent displacement. The comparison between the results obtained by applying directly the seismic input at the bedrock and those obtained by considering the site amplification effects shows that a significant underestimation of permanent displacements is to be expected if this aspect is not taken into account. In addition, it is worth noting that the effect of soil stiffness on the seismic performance of the structure can be significant, particularly for cases r05 and r06 with the lower critical accelerations, where $u_{x,\max}$ computed for site C is almost twice the corresponding value for site B. This is a result of the fact that the soil profile C tends to amplify the lower frequencies, while the most significant amplification effects on site B occur at relatively higher frequencies.

5. Comparison with non–linear dynamic FE simulations

The last FE–LA simulation of Tab. 1 (r07) has been performed to compare the predictions of the GNM with the results of non–linear dynamic FE analyses, to provide an assessment of its predictive capabilities as compared to more rigorous but computationally more demanding approaches. The non–linear dynamic simulations have been performed with the FE code Tochnog Professional [35].

5.1. Problem geometry, soil properties and seismic input adopted in the FE simulations

The excavation geometry for case r07 is characterized by the same dimensions adopted in the previous cases – height $h = 8.0$ m and width $b = 18$ m – but a smaller wall embedment depth ($d = 3.0$ m) has been chosen to obtain relatively low critical accelerations (see Tab. 2). The adopted yield bending moment for the walls is sufficiently high that no plastic hinges are formed at failure. Therefore, both the walls and the struts have been modeled as linear elastic structural elements.

A detail of the central portion of the discretization adopted in the FE simulations is shown in Fig. 14. The soil layer, 25 m thick, is discretized with 3900 bi–quadratic, 8–noded elements with 2 displacement dofs per node; the walls have been modeled with 88 beam elements and the strut with a single truss element. Particular care has been placed in the selection of the maximum element size to avoid filtering of high frequencies [36], taking into account the characteristics of the seismic input considered. Periodic boundary conditions have been assumed at the fictitious vertical boundaries of the domain, and a relatively large distance has been adopted between them and the diaphragm walls (90 m), in order to minimize the effects of possible spurious reflections.

In the FE simulations, the soil layer has been assumed as an elastic–perfectly plastic medium with a Mohr–Coulomb yield function and non–associative plastic flow. Although the material library of Tochnog Professional contains several

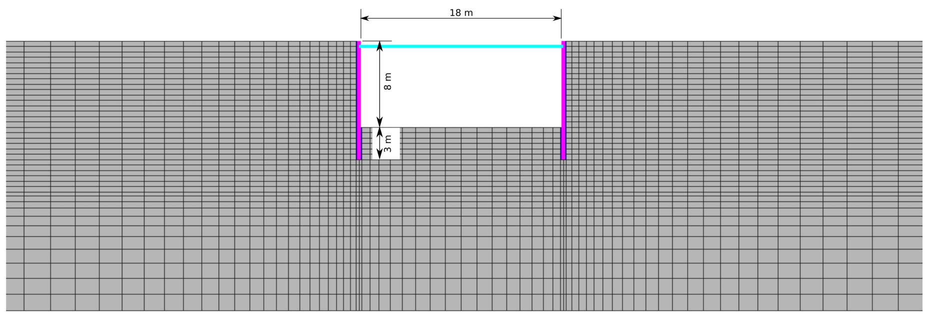

Figure 14: Detail of the discretization adopted in non–linear dynamic FE simulations (elements inside the excavation removed).

advanced material models for coarse–grained materials, in this case the choice of the relatively standard perfect plasticity model adopted in the simulations has been dictated by the need to guarantee the consistency between the FE simulations and the simplified GNM approach, in which permanent deformations are accumulated only when the system is in (instantaneous) global failure conditions.

The soil unit weight as well as the material constants defining the soil shear strength and dilatancy adopted in the simulations are provided in Tab. 1. The elastic behavior of the soil has been assumed isotropic and linear elastic, with shear and bulk stiffnesses provided by the following relation:

$$G(p) = G_{\text{ref}} \left(\frac{p}{p_{\text{ref}}} \right)^{\alpha} \qquad\qquad K(p) = \frac{2(1+\nu)}{3(1-2\nu)}\, G(p) \tag{25}$$

with $G_{\text{ref}} = 127$ MPa, $p_{\text{ref}} = 100$ kPa, $\alpha = 0.5$ and $\nu = 0.2$. The shear modulus is assumed to be equal to the small–strain shear stiffness G_0 of the soil. With the aforementioned properties, and adopting a coefficient of earth pressure at rest $K_0 = 0.5$ to define the geostatic stress state, eq. $(25)_1$ provides a small–strain shear stiffness profile corresponding to soil profile C of Sect. 4.1.

Two different seismic inputs have been considered in the dynamic FE simulations: the Poggio Cancelli earthquake of Tab. 3 (hereafter indicated as SI-1) and a slightly stronger earthquake obtained by amplifying the accelerations of the Poggio Cancelli signal by 40% (hereafter indicated as SI-2).

5.2. Selected results

Some selected results from the non–linear FE simulations with the inputs SI–1 and SI–2, along with the corresponding predictions provided by the GNM are shown in Figs. 15–17. All the figures focus on horizontal displacements, which, for the case at hand provide a reasonable indication of the overall system performance.

Fig. 15 shows the contour maps of post–seismic horizontal displacement u_x computed in the two non–linear dynamic simulations. The corresponding final permanent displacement fields obtained with GNM are plotted in Fig. 16. By comparing the two sets of results, it can be observed that the minimum and maximum horizontal displacements predicted by the FE simulations at the wall tips are captured quite reasonably by the GNM solutions, where $u_{x,\mathrm{min}}$ and $u_{x,\mathrm{max}}$ occur at the same points, see Tab. 5. Also, the entire spatial distributions of the permanent displacements provided by the two approaches look quite close in both cases, in spite of the strong simplifying assumptions introduced in the GNM. From the comparison of Figs. 15 and 16 and the data in Tab. 5 it can be noted that the agreement between GNM and FE displacements is better for the strongest earthquake SI–2, when both rightward and leftward plastic mechanisms are fully mobilized, than for the weakest earthquake SI–1, for which the leftward mechanism is not completely activated and the minimum displacement computed in the FE simulation for the right wall is only 37% of the corresponding GNM displacement.

The time evolutions of u_x in a point located on the left wall, at the base of the excavation, computed by the two approaches for the two seismic inputs are shown in Fig. 17. While it is clear that, in both cases, the permanent displacements are accumulated in correspondence to the peaks of the seismic excitations, the $u_x(t)$ curve provided by the GNM is not realistic, as it does not take into account the effects of the reversible component of the soil deformations during the events – responsible for the obscillations observed in the FE results. The only instant in which the comparison between the two simulations is meaningful is at the end of the earthquake event, when all the displacements observed in

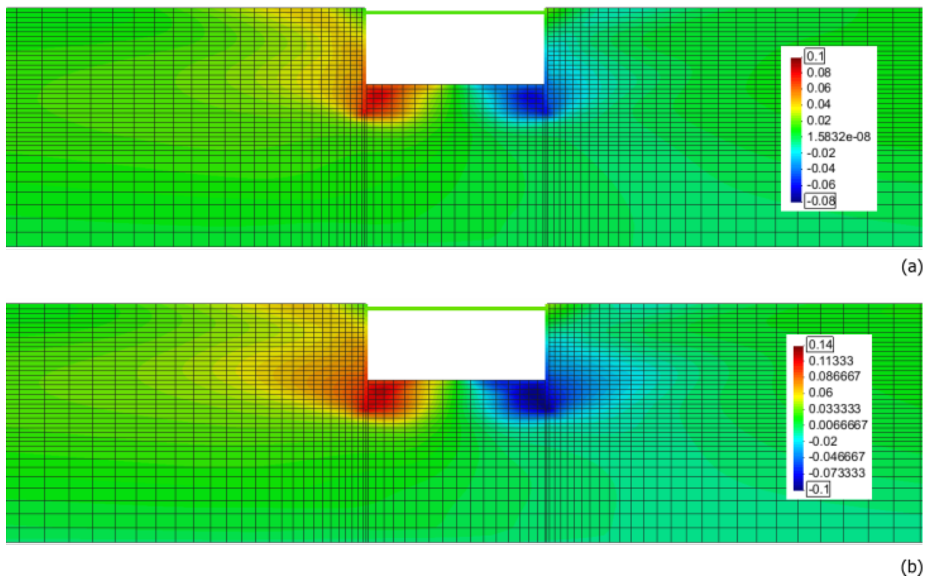

Figure 15: Contour maps of post–seismic horizontal displacement u_x computed by non–linear dynamic FE simulations: a) seismic input SI–1; b) seismic input SI–2.

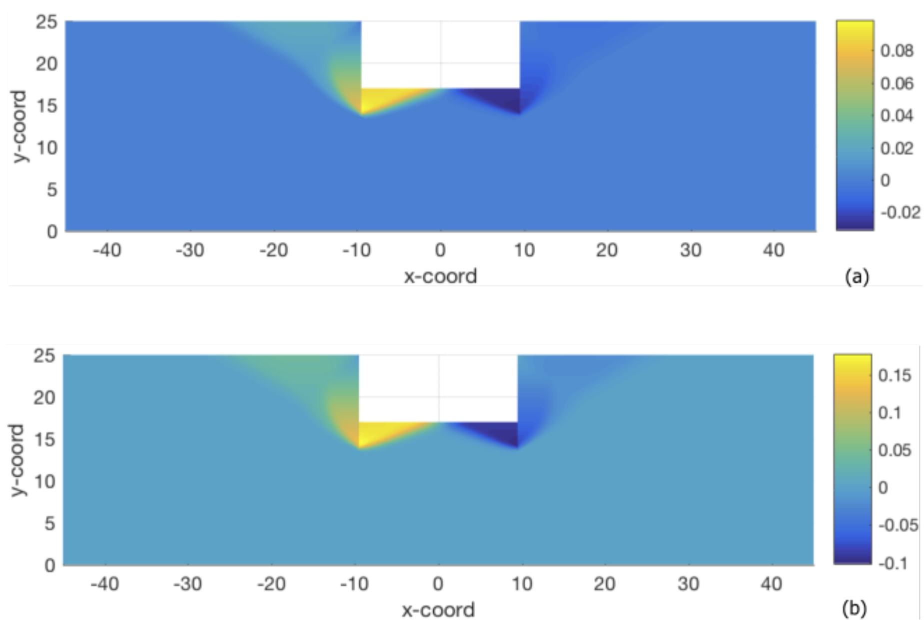

Figure 16: Contour maps of post–seismic permanent horizontal displacement u_x computed by the GNM: a) seismic input SI–1; b) seismic input SI–2.

Table 5: Maximum and minimum post–seismic horizontal displacements predicted with the FE and GN methods.

Seismic input	Type of simulation	$u_{x,\max}$ (m)	$u_{x,\min}$ (m)
SI–1	FEM	0.10	-0.08
SI–1	GNM	0.10	-0.03
SI–2	FEM	0.14	-0.10
SI–2	GNM	0.16	-0.10

the dynamic FE simulations are mostly the effect of irreversible deformation processes in the soil.

6. Concluding remarks

In this work, a Generalized Newmark Method has been proposed for estimating the permanent displacement field induced by seismic actions on geotechnical structures such as diaphragm walls propped at the crest. The method relies crucially on the results of quasi–static FE–LA simulations, which not only provide very accurate estimates of the critical acceleration for each possible orientation of the seismic action, but also very detailed information on the normalized velocity field associated to the collapse mechanism. The effects of local site amplification are taken into account by means of a simple, non–linear 1–d site response analysis.

The application of the GNM to a number of flexible retaining structures supporting a deep excavation in sand has shown that – depending on the embedment depth and strength of the soil and the walls – different collapse mechanisms can be activated which, in most cases, include both soil and wall yielding. In most cases, the collapse mechanisms activated by the leftward and rightward seismic actions are not independent, in the sense that the zones of soil interested by each

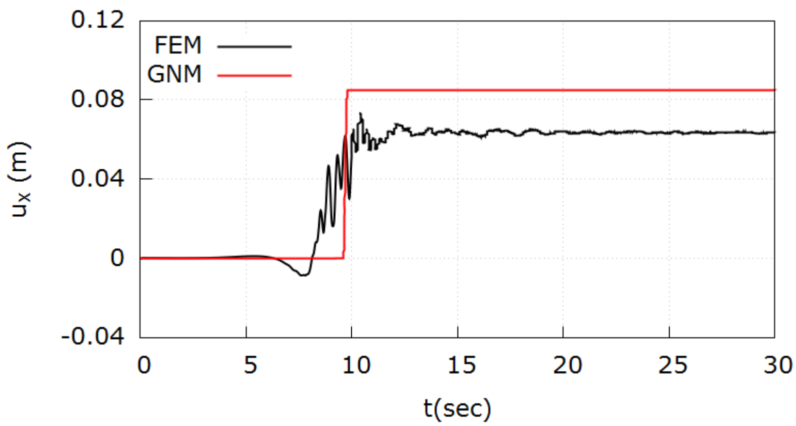

(a)

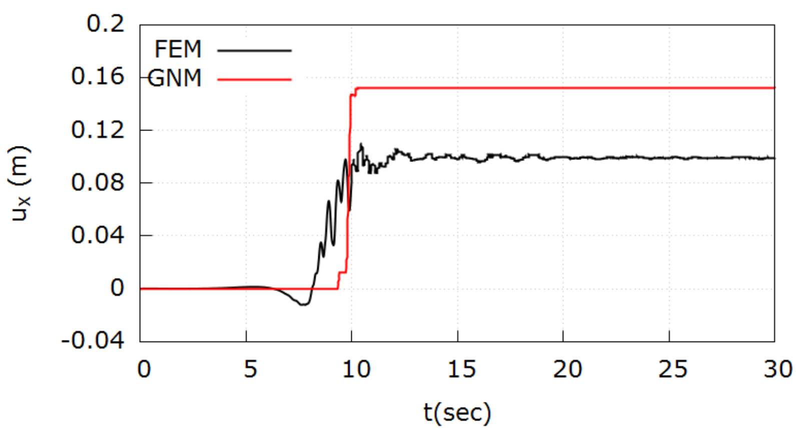

(b)

Figure 17: Time–histories of horizontal displacement of the left wall at the base of the excavation: a) seismic input SI–1; b) seismic input SI–2.

collapse mechanisms are not disjoint. Therefore, the permanent displacements in the areas affected by both collapse mechanisms must be determined by vectorially superimposing the effects of each failure mode. The Generalized Newmark Method can handle such feature of the collapse mechanisms in a straightforward way.

The proposed approach allows to take into account the effects of both soil strength, which controls the critical accelerations of the system, and soil stiffness and damping properties, which affect the seismic input provided by the 1–d site response analysis. This last aspect is particularly important as significant variations in the predicted performance of the structure can be obtained for different stiffness profiles, for a given seismic input at the bedrock.

The comparison between the permanent displacements fields provided by the GNM and those computed by means of non–linear, dynamic FE simulations for two different earthquake events have shown that the proposed approach can capture quite realistically, from both the qualitative and quantitative points of view, the post–seismic displacement field computed by taking rigorously into account all the balance principles and the constitutive equations of the continuous medium under the dynamic excitation. It is worth noting that the model adopted for the soil in the FE simulations is a relatively standard perfect plasticity model which, in general, is not capable of reproducing all the relevant features of the cyclic/dynamic behavior of the soil under seismic loading conditions. In this case, the choice has been dictated by the need to guarantee the consistency between the FE simulations and the simplified GNM approach, in which permanent deformations are accumulated only when the system is in (instantaneous) global failure conditions.

Further studies are currently in progress to validate the Generalized Newmark Method on both experimental data obtained in small–scale model tests under artificial gravity and non–linear FE simulations carried out with advanced constitutive models, capable of modeling plastic yielding even for stress paths which do not necessarily lead to material failure. As pointed out by Conti et al. [21], this will require the parallel introduction in the GNM of a suitable hardening mechanism for the critical acceleration a_c, by means of an evolution equation linking $\dot{a}_c$ with the permanent displacement rate. The extension of the GNM to incorporate such an effect and the studies necessary to properly define the features of the hardening law for a_c are currently under way, and will be presented in forthcoming publications.

Acknowledgements

The Authors would like to thank the two anonymous reviewers for their valuable comments to the original version of the manuscript, which have significantly improved the quality of the paper.

Bibliography

[1] S. Okabe. General theory of earth pressure. *J. Jpn. Soc. Civil Engng.*, 12, 1926.

[2] N. Mononobe and H. Matsuo. On the determination of earth pressures during earthquakes. In *Proceedings, World Engineering Congress*, volume 9, pages 179–187, 1929.

[3] CEN. Eurocode 8: Design of structures for earthquake resistance-part 5: Foundations, retaining structures and geotechnical aspects. 2003.

[4] Ministero delle Infrastrutture. *Decreto del 14/01/2008 – Norme Tecniche per le Costruzioni*. Gazzetta Ufficiale della Repubblica Italiana (in Italian), 2008.

[5] S. Iai, K. Ichii, H. Liu, and T. Morita. Effective stress analyses of port structures. *Soils and Foundations*, 38:97–114, 1998.

[6] M. Alyami, S. M. Wilkinson, M. Rouainia, and F. Cai. Simulation of seismic behaviour of gravity quay wall using a generalized plasticity model. In *Proceedings of the 4th international conference on earthquake geotechnical engineering, Thessaloniki, Greece*, 2007.

[7] C. Miriano, E. Cattoni, and C. Tamagnini. Advanced numerical modeling of seismic response of a propped rc diaphragm wall. *Acta Geotechnica*, 11(1):161–175, 2016.

[8] E. Cattoni and C. Tamagnini. On the seismic response of a propped r.c. diaphragm wall in a saturated clay. *Acta Geotechnica*, (submitted), 2018.

[9] B. Becci and R. Nova. Un metodo di calcolo automatico per il progetto di paratie. *Rivista Italiana di Geotecnica*, 21(1):33–47, 1987.

[10] P. Franchin, P. E. Pinto, and F. Noto. A simplified nonlinear dynamic model for seismic analysis of earth-retaining diaphragm-walls. In *4th Intnl. Conf. Earthq. Geotech. Engng., Thessaloniki, Greece (paper 1220)*, 2007.

[11] P. Franchin and F. Cavalieri. Seismic performance–based design of flexible earth-retaining diaphragm walls. *Engineering Structures*, 78:57–68, 2014.

[12] P. Franchin and P. E. Pinto. Performance–based seismic design of integral abutment bridges. *Bulletin of earthquake engineering*, 12(2):939–960, 2014.

[13] N. M. Newmark. Effects of earthquakes on dams and embankments. *Géotechnique*, 15(2):139–160, 1965.

[14] R. V. Whitman. Seismic design and behavior of gravity retaining walls. In *Design and performance of earth retaining structures*, pages 817–842. ASCE, 1990.

[15] X. Zeng and R. S. Steedman. Rotating block method for seismic displacement of gravity walls. *J. of Geotech. and Geoenv. Engng., ASCE*, 126(8):709–717, 2000.

[16] D. Choudhury and S. Nimbalkar. Seismic rotational displacement of gravity walls by pseudodynamic method. *Int. J. of Geomechanics, ASCE*, 8(3):169–175, 2008.

[17] B. M. Basha and G. L. Sivakumar Babu. Seismic rotational displacements of gravity walls by pseudodynamic method with curved rupture surface. *Int. J. of Geomechanics, ASCE*, 10(3):93–105, 2010.

[18] D. G. Elms and R. Richards. Seismic design of retaining walls. In *Design and performance of earth retaining structures*, pages 854–871. ASCE, 1990.

[19] R. Richards and D. G. Elms. Seismic passive resistance of tied-back walls. *J. of Geotech. Engng., ASCE*, 118(7):996–1011, 1992.

[20] L. Callisto and F. M. Soccodato. Seismic design of flexible cantilevered retaining walls. *J. of Geotech. and Geoenv. Engng., ASCE*, 136(2):344–354, 2010.

[21] R. Conti, G. S. P. Madabhushi, and G. M. B. Viggiani. On the behaviour of flexible retaining walls under seismic actions. *Géotechnique*, 62(12):1081, 2012.

[22] R. Conti and G. M. B. Viggiani. A new limit equilibrium method for the pseudostatic design of embedded cantilevered retaining walls. *Soil Dyn. and Earthquake Engng.*, 50:143–150, 2013.

[23] R. Conti, G. M. B. Viggiani, and F. Burali D'Arezzo. Some remarks on the seismic behaviour of embedded cantilevered retaining walls. *Géotechnique*, 64(1):40, 2014.

[24] E. Cattoni and C. Tamagnini. Using FE limit analysis to evaluate permanent displacements of geotechnical structures under seismic conditions. *Journal of Earthquake Engineering*, page (in press; doi: 10.1080/13632469.2018.1452805), 2018.

[25] R. Villaverde. Methods to assess the seismic collapse capacity of building structures: State of the art. *Journal of Structural Engineering*, 133(1):57–66, 2007.

[26] C. A. Goulet, C. B. Haselton, J. Mitrani-Reiser, J. L. Beck, G. G. Deierlein, K. A. Porter, and J. P. Stewart. Evaluation of the seismic performance of a code-conforming reinforced-concrete frame building?from seismic hazard to collapse safety and economic losses. *Earthquake Engineering & Structural Dynamics*, 36(13):1973–1997, 2007.

[27] S. W. Sloan. Substepping schemes for the numerical integration of elasto-plastic stress–strain relations. *Int. J. Num. Meth. Engng.*, 24(5):893–911, 1987.

[28] S. W. Sloan. Lower bound limit analysis using finite elements and linear programming. *Int. J. Num. Anal. Meth. Geomech.*, 12(1):61–77, 1988.

[29] K. Krabbenhoft, A.V. Lyamin, and J. Krabbenhoft. *Optum^{G2}: Theory Manual*. Optum Computational Engineering, 2015.

[30] K. Krabbenhoft, M. R. Karim, A. V. Lyamin, and S. W. Sloan. Associated computational plasticity schemes for nonassociated frictional materials. *International Journal for Numerical Methods in Engineering*, 90(9):1089–1117, 2012.

[31] L. Luzi, F. Pacor, and R. Puglia. Italian accelerometric archive v2.1. istituto nazionale di geofisica e vulcanologia. Technical report, Dipartimento della Protezione Civile Nazionale, 2016.

[32] J. P. Bardet, K. Ichii, and C. H. Lin. *EERA: a computer program for equivalent-linear earthquake site response analyses of layered soil deposits.* University of Southern California, Department of Civil Engineering, 2000.

[33] R. O. Hardin and V. P. Drnevich. Shear modulus and damping in soils: design equations and curves. *Journal of Soil Mechanics & Foundations Div*, 98(sm7), 1972.

[34] I. Ishibashi and X. Zhang. Unified dynamic shear moduli and damping ratios of sand and clay. *Soils and Foundations*, 33(1):182–191, 1993.

[35] D. Roddeman. *Tochnog Professional users manual.* Finite Element Application Technology (FEAT), the Netherlands., 2018.

[36] R. L. Kuhlemeyer and J. Lysmer. Finite element method accuracy for wave propagation problems. *Journal of Soil Mechanics & Foundations Div*, 99(Tech Rpt), 1973.